Available online at www.sciencedirect.com
SCIENCE DIRECT®
ELSEVIER
International Journal of Refrigeration 28 (2005) 1006–1017
REVUE INTERNATIONALE DU FROID
INTERNATIONAL JOURNAL OF
refrigeration
www.elsevier.com/locate/ijrefrig

Air-side heat transfer enhancement of a refrigerator evaporator using vortex generation

A.D. Sommers*, A.M. Jacobi

Department of Mechanical and Industrial Engineering, University of Illinois, 1206 W. Green Street, Urbana, IL 61801, USA

Received 15 September 2004; received in revised form 17 February 2005; accepted 1 April 2005
Available online 15 June 2005

Abstract

In most domestic and commercial refrigeration systems, frost forms on the air-side surface of the air-to-refrigerant heat exchanger. Frost-tolerant designs typically employ a large fin spacing in order to delay the need for a defrost cycle. Unfortunately, this approach does not allow for a very high air-side heat transfer coefficient, and the performance of these heat exchangers is often air-side limited. Longitudinal vortex generation is a proven and effective technique for thinning the thermal boundary layer and enhancing heat transfer, but its efficacy in a frosting environment is essentially unknown. In this study, an array of delta-wing vortex generators is applied to a plain-fin-and-tube heat exchanger with a fin spacing of 8.5 mm. Heat transfer and pressure drop performance are measured to determine the effectiveness of the vortex generator under frosting conditions. For air-side Reynolds numbers between 500 and 1300, the air-side thermal resistance is reduced by 35–42% when vortex generation is used. Correspondingly, the heat transfer coefficient is observed to range from 33 to 53 W m^{-2} K^{-1} for the enhanced heat exchanger and from 18 to 26 W m^{-2} K^{-1} for the baseline heat exchanger.

Keywords: Domestic refrigeration; Display cabinet; Evaporator; Improvement; Heat transfer; Air; Finned tube; Vortex

Amélioration du transfert de chaleur côté air à l'aide d'un évaporateur utilisant un système de génération de vortex

Mots clés : Froid domestique ; Meuble de vente ; Évaporateur ; Amélioration ; Transfert de chaleur ; Air ; Tube aileté ; Vortex

1. Introduction

Plain-fin-and-tube heat exchangers having a large fin spacing (i.e. 5–10 mm) are used in certain frosting applications because of their reliability, cost-effectiveness, and relative tolerance to frost accumulation. Unfortunately, this heat exchanger geometry is thermally inefficient, and the air-side convective coefficients are relatively small in comparison to more highly compact designs and interrupted fin designs. The constraints imposed on the design of these heat exchangers require new and innovative approaches to further reduce the core volume, material cost, and flow noise. Because the air-side thermal resistance is dominant in these applications, even modest enhancements in the air-side thermal–hydraulic performance could lead to smaller,

* Corresponding author. Tel.: +1 217 244 0778; fax: +1 217 244 6534.
E-mail address: asommers@uiuc.edu (A.D. Sommers).

0140-7007/$35.00 © 2005 Elsevier Ltd and IIR. All rights reserved.
doi:10.1016/j.ijrefrig.2005.04.003

Nomenclature

A	area
b	delta wing span
c	delta chord span, or specific heat
C	heat-rate capacity, $\dot{m}c_p$
D	diameter
f	Fanning friction factor, $((2\Delta P_{core}\rho_{air})/G^2)(A_{min}/A_{tot})$
G	mass velocity, ρV_{max}
h	heat transfer coefficient, or enthalpy
j	Colburn j-factor, $Nu/(RePr^{1/3})$
k	thermal conductivity
L	fin length (flow depth)
Le	Lewis number for water in air (α/D_{ab})
$\dot{m}$	mass flow rate
mf	water vapor mass fraction
N	number of tubes, fins, etc.
Nu	tube-side Nusselt number, hD/k
NTU	number of transfer units (UA/C_{min})
$\dot{P}$	pumping power
Pr	Prandtl number, $(\rho\nu c_p)/k$
ΔP	pressure drop
q	rate of heat transfer
R	thermal resistance, or ratio of heat-rate capacity (min/max)
Re_{Dh}	air-side Reynolds number, $V_{max}D_h/\nu$
t	time
T	temperature
UA	thermal conductance
V	velocity or volume

Greek symbols

α	thermal diffusivity of moist air, angle of attack
δ	frost thickness
ε	heat exchanger effectiveness, q/q_{max}
ν	kinematic viscosity
Θ	modified volume-goodness factor, $q_{air}/(V_{core}\Delta h_{lm})$
Λ	delta wing aspect ratio
ρ	density
ω	humidity ratio

Subscripts

1,2	pass
air	for air
C	ratio of heat capacity rates, min/max
core	for the heat exchanger
down	downstream of the heat exchanger
f	frost
fin	fin
h	hydraulic ($D_h = 4A_{min}L/A_{tot}$)
i	inlet
m	middle
lm	log-mean difference
max	maximum
min	minimum
o	outer
p	tube pass
r	refrigerant flow
s	at the frost surface
t	tube wall
tube	for a tube
tot	total for air-side heat transfer
up	upstream of the heat exchanger
w	water

lighter, quieter, and more energy-efficient systems. The purpose of this research is to provide an assessment and understanding of the promise of vortex generators (VGs) as an air-side enhancement technique for heat exchangers with large fin spacing in frosting applications. Specific objectives of this study include evaluating the performance of delta-wing vortex generators under low air flow rates, their efficacy downstream from the leading edge, and their tolerance to frost accumulation. Frost properties are evaluated by calculating a time-varying interfacial surface temperature, and the frost thickness is found by numerically integrating mass deposition rate data from the wind tunnel.

Streamwise vortex enhancement works by imparting a secondary flow to the main flow; specifically a vortex is formed and it interacts with the boundary layer on the surface of the fin. The downwash region of the vortex thins the thermal boundary layer; whereas, the upwash region thickens it. These surface-normal inflow and outflow regions occupy nearly the same surface area, but the convective response is nonlinear and a net heat transfer enhancement is manifest. This enhancement comes at the cost of an increased pressure drop, due to the form drag on the vortex generators, but this incremental increase in pressure drop is relatively small for a plain-fin-and-tube heat exchanger where a major source of drag is the tubes.

Several individuals have demonstrated the clear promise vortex generation has as a heat transfer enhancement method. For instance, in a review of the technical literature, Fiebig [1] concluded that local heat transfer enhancements of 100% and overall enhancements of 50% were possible. He also reported that vortex generators inserted into channel flow might produce turbulent flow instabilities for Reynolds numbers as low as 350. In a recent study using delta winglets, Kwak et al. [2] observed heat transfer improvements of 10–25% with a corresponding increase in pressure losses of 20–35% in a multi-channel test core using a three-row, circular tube bundle in an in-line arrangement. Full-scale implementation and testing of vortex generators in heat exchangers, however, is only sparsely reported in the literature. In one test performed by Russell et al. [3] using

rectangular winglets, the j factor was enhanced by 47% while the f friction factor increased by 30% for a Reynolds number of 500 based on hydraulic diameter. A second, more recent full-scale test of delta-wing vortex generators on a plain-fin-and-tube heat exchanger was conducted by ElSherbini and Jacobi [4], and they showed considerable heat transfer augmentation with little to no pressure drop penalty. For the present study, the dimensions and angle of attack of the VG array were selected on the basis of an extensive parametric study performed by Gentry and Jacobi [5] for a single delta wing in developing channel flows.

Aside from early work by Storey and Jacobi [6] for a channel flow, we are aware of no research reported in the open literature on the use of vortex generators with simultaneous heat and mass transfer, where the accumulating frost can change the geometry of the vortex generator and affect the flow of the air stream as shown in Fig. 1. On the other hand, there is an extensive body of technical literature on frost in general, and a significant body of work on frost growth on heat exchangers. The literature on frost is so extensive that we will focus our discussion on only the articles highly germane to the current study.

Östin and Andersson [7] concluded that the substrate temperature and the relative humidity of the air stream both have important effects on the frost thickness, but the contribution of the air velocity to frost thickness is negligible. They also observed monotonic and cyclic growth patterns and found that for times greater than 60 min, the contribution of the mass flux of condensed vapor that went towards increasing the frost thickness varied between 0.41 and 0.65 with an average value of 0.49. This finding suggests that mass transfer to the frost layer contributes nearly equally to the increase of frost density and frost thickness, as previously suggested by White and Cremers [8].

With respect to experimental methods in the study of frosted heat exchangers, Rite and Crawford [9] explored ways of directly and indirectly measuring the frosting rate, and their work suggests that a frost deposition rate measured indirectly from experimentally collected upstream and downstream relative humidities can provide reliable data. In a separate paper, Rite and Crawford [10] found that while holding the air flow rate constant, the overall thermal conductance increased as frost was deposited on the coil, a phenomenon they attributed to an increased heat transfer coefficient and added surface roughness from the frost. They also determined that the deposition of frost in the gaps between the evaporator tube and mechanically joined fins only negligibly decreases the contact resistance during normal operation.

More recently, Cheng and Cheng [11] proposed a theoretical model for predicting the frost growth rate on a flat plate based on the mass and energy conservation laws and the Hayashi [12] correlation for finding frost density. Their model is useful for calculating the growth rate of the frost layer during the mature growth period as well as predicting the onset of frost melting. Le Gall and Grillot [13], in deriving a one-dimensional transient model for the prediction of frost growth and densification on a cold surface, observed that the transport of water vapor into the frost layer was often significantly higher than that due to simple Fickian diffusion. To better represent this phenomenon, they developed a new expression for the so-called diffusion resistance factor and suggested that these greater mass diffusivities might be due to phase change kinetics, thermophoresis, or other secondary effects. Several other studies of frost growth related to the current work should also be noted (Mago and Sherif [14]; Ogawa, Tanaka, and Takeshita [15]; Schneider [16]; Tao, Besant, and Rezkallah [17]; and Inaba and Imai [18]).

2. Experimental method

2.1. Air-side loop

The experiments were conducted in a closed-loop wind tunnel comprised of five major sections: a thermal-conditioning chamber, flow-conditioning chamber, contraction, test section, and return loop as shown in Fig. 2 and detailed by Davis and co-workers [19]. The temperature and humidity of the air were established inside the thermal-

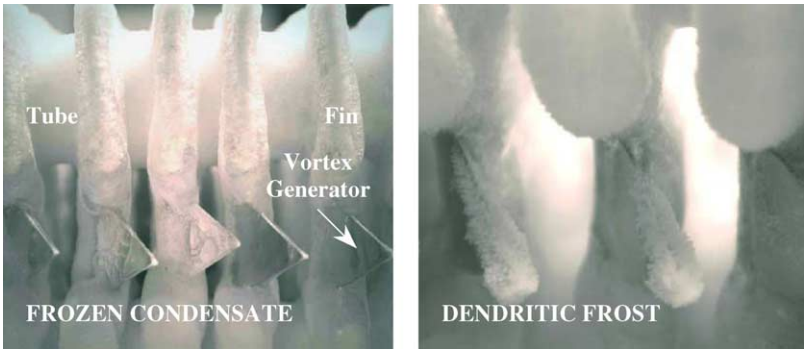

Fig. 1. Frost deposition on delta wing-type vortex generators.

conditioning chamber prior to each experiment using an upstream cooling coil and a controlled steam injection system. The relative humidity in the wind tunnel was preset to 80% before each experimental run, and the air inlet temperature was preconditioned to be between 10 and 11 °C. Accompanying air outlet temperatures ranged from −4 to 2 °C. The core pressure drop across the heat exchanger was measured using 4 pressure taps (2 upstream and 2 downstream). An electronic manometer with measurement uncertainty of ±0.25 Pa was used to measure the pressure drop under dry conditions, and a 250 Pa pressure transducer with an uncertainty of 0.073% full-scale was used to measure the pressure drop of the heat exchanger under frost conditions. Because the minimum detectable pressure difference for these instruments was 0.25 and 0.18 Pa, respectively, very small core pressure drop measurements could be recorded. Air inlet and outlet temperatures were measured using thermopiles placed upstream and downstream of the exchanger. These thermopiles were inserted from both the top and bottom surface of the test section and consisted of five 0.25-mm-diameter, type-T thermocouples calibrated against NIST-traceable ASTM thermometers. Because each thermopile represented a spatial average of five individual thermocouples and multiple thermopiles were used upstream and downstream, highly accurate temperature measurements were possible. The resulting uncertainty in the average air temperature from the performed calibration was within ±0.1 °C with 95% confidence. The velocity of the approach air was measured using hot-bulb anemometry with a maximum uncertainty of approximately ±0.06 m s^{-1}. The velocity profiles were shown to be flat within ±4.3% for the lowest test velocity (0.46 m s^{-1}) and ±5.7% for the highest test velocity (2.0 m s^{-1}).

2.2. Coolant loop

The refrigerant was a 40% mixture by weight of ethylene glycol (DOWTHERM 4000) and water. The inlet and outlet fluid temperatures were measured using platinum RTDs with an uncertainty of ±0.017 °C. The coolant inlet temperature was maintained at −12 to −13 °C for each experiment. Mixing cups and 90° elbows were incorporated into the piping network upstream of the RTDs to ensure a well mixed, bulk fluid temperature. A Coriolis-effect flow meter was installed downstream from the heat exchanger to measure the coolant mass flow rate with an uncertainty of ±0.4%.

The heat exchanger specimen used for conducting this comparison was of a plain-fin-and-tube construction with a fin spacing of 8.47 mm, where the fins were brazed to the tube in order to eliminate thermal contact resistance. The dimensions of the heat exchanger were 451×203×51 mm^3, and the hydraulic diameter before frosting was 10.2 mm. Heat transfer data from the exchanger were acquired every 5 min following an initial frost growth period of 30 min. For enhanced testing, vortex generators were attached to the fin surface of the heat exchanger according to the pattern shown in Fig. 3.

2.3. Vortex generator geometry

The delta-wing vortex generators used in the enhanced testing were cut from standard 0.25 mm aluminum shim

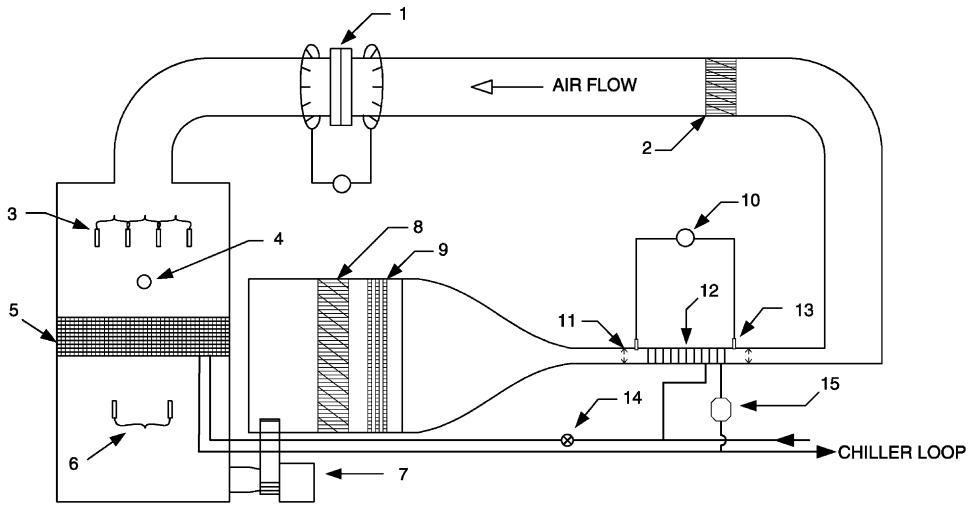

1. Orifice plate
2. Honeycomb
3. Pre-heaters
4. Steam injection
5. Cooling coils
6. After-heaters
7. Blower
8. Honeycomb
9. Screens
10. Pressure transducer
11. Thermopiles
12. Test section
13. Pressure taps
14. Control valve
15. Coriolis flow meter

Fig. 2. Wind tunnel schematic with descriptors.

stock, using wire electrical discharge machining (EDM). They were made with an aspect ratio, Λ, of 2.0 and placed on the heat exchanger with an angle of attack, α, of approximately 55°. They were attached to the fin surface at intervals of 51 mm using double-sided tape. The addition of the vortex generators to the heat exchanger only accounted for 3.1% of the total possible surface area. All relevant wing dimensions are provided below in Fig. 4.

3. Data interpretation

Energy balances were monitored to ensure fidelity of all measured data. For 80% of the data points reported, the maximum energy transfer difference was 8.3% while the remaining 20% of the data had energy balances between 8.4 and 10%. The energy balance discrepancies are largely attributable to the uncertainties in measuring the heat transfer rate from the air, which typically range from 3 to 5% compared to only 1–3% for the coolant side. An ε-NTU method was then utilized to interpret the performance of the heat exchanger. For the geometry studied, the exchanger could be divided into two partitions along an adiabat with each partition containing eight passes in cross-flow. The upper partition (stream 1) had an overall counter flow arrangement while the lower partition (stream 2) had an overall parallel flow arrangement. Total energy balances were written for each partition and each stream, and two ε-NTU equations were used to complete the system of equations, following an approach similar to that used by Davis [19]. In the ε-NTU equations, the maximum realizable enthalpy difference was written for the air stream in each partition. For the counter flow partition, the enthalpy of the exiting air stream represents the minimum achievable air enthalpy, corresponding to the known coolant inlet temperature, T_{ri} and a relative humidity value of unity. For the parallel flow partition, the enthalpy of the exiting air stream represents the minimum achievable air enthalpy, corresponding to the calculated midstream coolant temperature, T_{rm} and a relative humidity value of unity. Appropriate relations for the counter-flow partition effectiveness ε_1 and the parallel flow partition effectiveness ε_2 have been given by Shah and Mueller [20], and these values could be related to the pass effectiveness ε_p for simple cross flow with the heat rate capacity C_{min} mixed and C_{max} unmixed to calculate the number of transfer units per pass, NTU_P. Thus, the thermal conductance per pass, UA_P, could be determined, and the total thermal conductance, UA_{tot}, could be found by summing over all passes. These relationships are repeated here for completeness

$$\varepsilon_1 = \frac{\left(\frac{1-\varepsilon_p R_C}{1-\varepsilon_p}\right)^n - 1}{\left(\frac{1-\varepsilon_p R_C}{1-\varepsilon_p}\right)^n - R_C} \tag{1}$$

$$\varepsilon_2 = \frac{1-(1-\varepsilon_p(1+R_C))^n}{1+R_C} \tag{2}$$

$$\varepsilon_p = \frac{\{1-\exp[-R_C(1-\exp(-NTU_P))]\}}{R_C} \tag{3}$$

$$NTU_P = \frac{UA_P}{C_{min,P}} \tag{4}$$

$$UA_{tot} = UA_P \sum_{i=1}^{N} n_i \tag{5}$$

where n is the number of passes in each partition and N is the total number of passes.

The total thermal resistance, R_T, which equals $1/UA_{tot}$, can in turn be represented as a series of individual resistances equivalent to the sum of the refrigerant convection resistance ($R_{r\text{-}conv}$), tube wall conduction resistance ($R_{t\text{-}cond}$), frost conduction resistance (R_{frost}), and air-side convection resistance, (R_{as}), where the frost resistance and air-side resistance are each independently comprised of parallel resistances contributed by the tube and fin. The tube-side convection resistance was found using the Gnielinski correlation and the Colebrook correlation because of their suitability for the range of tube-side Reynolds numbers in these experiments. The frost conduction resistance was approximated using the Hayashi [12] correlation for frost density,

$$\rho_f = 650 \exp(0.277 T_s) \tag{6}$$

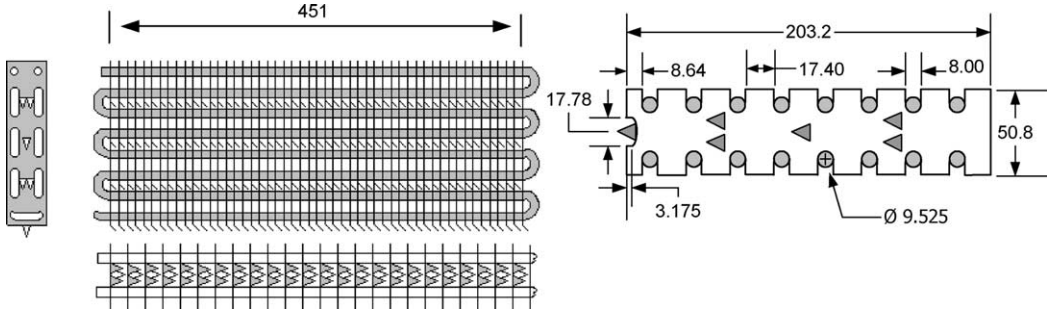

Fig. 3. Heat exchanger geometry and vortex generator configuration.

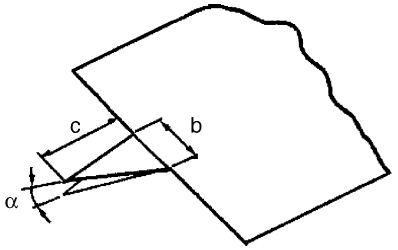

Wing span, b (mm)	10.5
Wing chord, c (mm)	10.5
Chord to hydraulic dia.	1.027
Aspect ratio, Δ=2b/c	2.0
Angle of attack, α	55°

Fig. 4. A vortex generator of chord length, c, base length, b, and angle of attack, α.

Lee et al. [21] correlation for frost thermal conductivity,

$$k_f = 0.132 + 3.13(10^{-4})\rho_f + 1.6(10^{-7})\rho_f^2 \tag{7}$$

and the following equations:

$$\frac{1}{R_f} = \frac{k_f A_{fin}}{\delta_f} + \frac{2\pi L_{tube} N_{tubes} k_f}{\ln((D_0 + 2\delta_f)/D_0)} \tag{8}$$

$$\dot{m}_f = \dot{m}_{air,up}\mathrm{mf}_{w,up} - \dot{m}_{air,down}\mathrm{mf}_{w,down} \tag{9}$$

$$\delta_f = \int_0^t \frac{\dot{m}_f}{(A_{tot}\rho_f)}\mathrm{d}t \tag{10}$$

where $\mathrm{mf}_{w,up}$ and $\mathrm{mf}_{w,down}$ represent the mass fractions of the water measured in the air upstream and downstream respectively, T_s represents an indirectly obtained interfacial surface temperature of the frost, and δ_f represents the frost thickness. From this information, the reciprocal of the refrigerant Nusselt number was plotted along the abscissa, and the total thermal resistance R_T at fixed air-side conditions was plotted along the ordinate to form a so-called Wilson plot. A line was then fit to the data by the method of least-squares, and the overall air-side resistance of the heat exchanger was inferred from a Wilson plot by extrapolating to the ordinate intercept. Here the tube-side refrigerant Nusselt number is infinite (i.e. $1/Nu_R = 0$) so the tube-side convection resistance is zero by definition. As a result, the intercept equals the air-side convective resistance plus the conduction resistance contributed by the frost and the tube wall—both known quantities. Because the tube wall conduction resistance is negligible, the frost resistance can be added to the convective resistance to form an overall air-side thermal resistance, which serves as a convenient basis of comparison for these tests.

Frost properties were evaluated using an average frost surface temperature, T_s, inferred using the heat-and-mass transfer analogy by relating the frost mass deposition rate (a known quantity) to the log-mean humidity ratio difference between the air and the frost surface. In this way, the humidity ratio, ω_s, (and hence temperature T_s) at the frost surface could be calculated using the following relationship

$$\dot{m}_f = \frac{h}{c_{p,air}} A_{tot} Le^{-2/3} \Delta\omega_{lm} \tag{11}$$

where

$$\Delta\omega_{lm} = \frac{(\omega_{up} - \omega_s) - (\omega_{down} - \omega_s)}{\ln[(\omega_{up} - \omega_s)/(\omega_{down} - \omega_s)]} \tag{12}$$

and Le is the Lewis number and A_{tot} is the total heat transfer surface area. In this way, T_s represents an indirectly measured quantity and should not be confused for a direct measurement.

Various performance evaluation criteria (PEC) were also calculated and used to assess the merits of vortex generation as a heat transfer enhancement technique. The Colburn j factor was used to represent dimensionless heat transfer and is defined as

$$j = \frac{h}{G c_{p,air}} \mathrm{Pr}_{air}^{2/3} \tag{13}$$

where h is the heat transfer coefficient and G is the mass velocity. Similarly, the friction factor, f, defined as

$$f = \frac{2\Delta P_{core}\rho_{air}}{G^2}\left(\frac{A_{min}}{A_{tot}}\right) - (1+\sigma^2)\left(\frac{\rho_{air,up}}{\rho_{air,down}} - 1\right)\left(\frac{A_{min}}{A_{tot}}\right)\left(\frac{\rho_{air,avg}}{\rho_{air,up}}\right) \tag{14}$$

where σ is the ratio of the minimum free flow area to the frontal area was used to nondimensionalize the pressure drop penalty. The London area-goodness factor, which is defined as the ratio of the Colburn j factor over the friction factor, f, is an often used metric in gauging the relative differences between heat exchangers; however, the use of j/f is restrictive because it does not explicitly account for blower power. Therefore, the final performance evaluation criterion used in this study was the modified volume-goodness factor, Θ. Formally, this PEC is defined as

$$\Theta = \frac{q}{(V_{core}\Delta h_{lm})} \tag{15}$$

where V_{core} is the exchanger core volume, q is the heat transfer rate of the air stream, and Δh_{lm} is the log-mean enthalpy difference. It is common to plot Θ against the blower power required to overcome the core pressure drop, ΔP_{core}.

4. Results and discussion

The thermal hydraulic performance of the evaporator was measured before and after the addition of the delta-wing vortex generators. In order to assess the pressure drop penalty associated with the enhanced geometry, the delta wing array was tested over several airflow rates under dry conditions. The results in Fig. 5 reveal a pressure penalty associated with the delta wings under dry conditions that varies between 17% for $Re_{Dh}=430$ and 67% for $Re_{Dh}=2270$ with an uncertainty in the measurements of 30.4 and 1.9%, respectively. The additional core pressure drop (i.e. 0.1–6.42 Pa) generated by the vortex generators over this range of Reynolds numbers, however, is small compared to overall system losses, and it should be noted that the incremental fan power needed to overcome this deficit would always be less than 0.31 W when using this enhanced geometry under dry conditions. These trends are also reflected in the air-side friction factor under dry conditions shown in Fig. 6. For frost conditions, the pressure drop penalty due to the VGs was obfuscated by the pressure drop penalty due to the growing frost layer. Under these conditions, the enhanced geometry and the baseline geometry were shown to have nearly identical core pressure drop penalties as seen in Fig. 7. This result suggests that vortex generators used in refrigeration applications may not suffer as severely from the usual drag penalties that are incurred under dry conditions.

For $500<Re_{Dh}<1300$, a consistent reduction of 35.0–42.1% in the overall air-side thermal resistance was observed for the enhanced evaporator as shown in Fig. 8. The uncertainty in overall air-side thermal resistance was conservatively calculated to range from 14 to 29% for these experiments and was due largely to uncertainties in the linear regression analysis used in the Wilson plot method. (As discussed in the methodology, the overall air-side resistance is the sum of the conduction resistance due to the frost and the convective resistance due to the air stream and therefore reflects the total effect that vortex generation has on both the growth of the frost layer and the thermal boundary layer at the surface.) These resistance values are significantly higher than those reported by El Sherbini and Jacobi [4] for a brazed evaporator of similar construction. The air-side resistances of his baseline data varied from 0.013 to 0.018 kW^{-1} over a similar range of Reynolds numbers. These discrepancies can be explained by recognizing that his fin pitch was nearly half of the current one

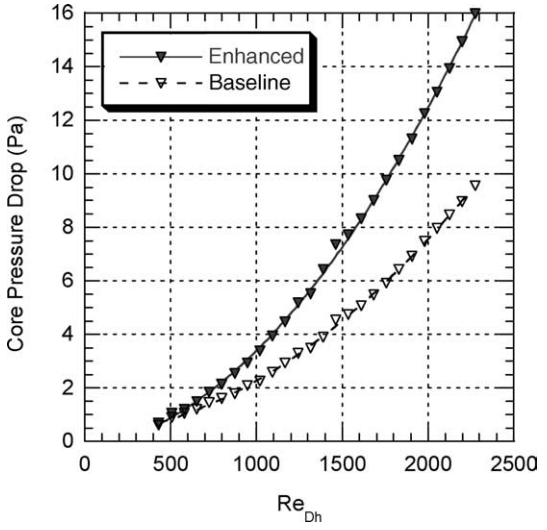

Fig. 5. Pressure drop penalty associated with using the vortex generator array under dry conditions.

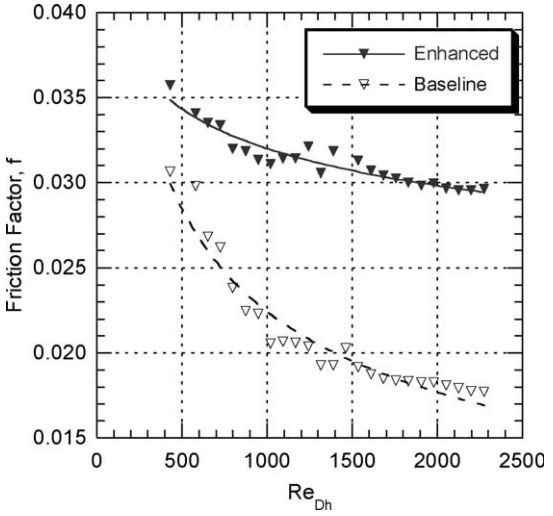

Fig. 6. Friction factor associated with using the vortex generator array under dry conditions.

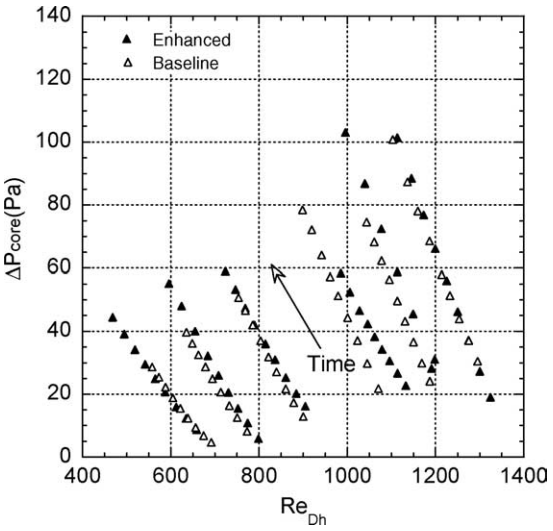

Fig. 7. Pressure drop penalty associated with using the vortex generator array under frost conditions. Each pair of curves represents a different initial face velocity testing condition.

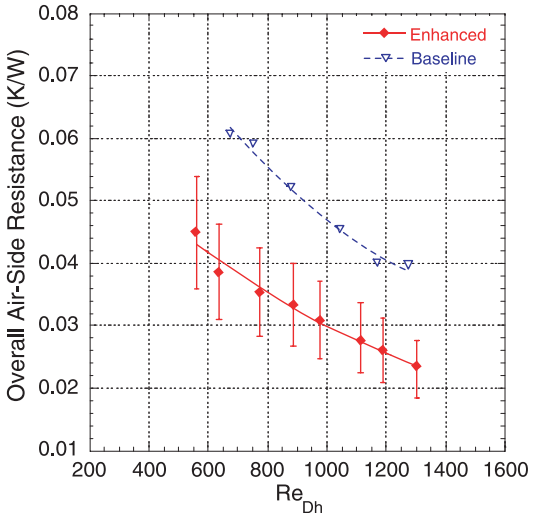

Fig. 8. The overall air-side thermal resistance is 35–42% lower for the enhanced evaporator under frost conditions.

being studied, and his tests were all conducted under dry conditions (i.e. no frost).

The reduction in air-side resistance can be largely ascribed to increased convection and flow mixing in the finned channels and is reflected in the behavior of the convective heat transfer coefficient, which was observed to increase by 60–93% over the range of tested air velocities as shown in Fig. 9. Because nonconducting tape was used to attach the delta wings, and the wing-to-fin area ratio was 1.9%, these enhancements can be entirely attributed to the streamwise vortices. The value of the heat transfer coefficient varied from 33 to 53 $W\,m^{-2}\,K^{-1}$ for the enhanced configuration and from 18 to 26 $W\,m^{-2}\,K^{-1}$ for the baseline configuration; typical uncertainties in heat transfer coefficient ranged from about 7–35%.

The observed increase in the air-side heat transfer coefficient with respect to time is best attributed to the growing frost layer and a few effects associated with it. First, the frost provides an added roughness to the surface area of the evaporator, which may serve to 'trip' the boundary layer from laminar to turbulent flow more quickly than a smooth surface. The consequence of turbulent flow is higher Nusselt numbers and delayed boundary layer separation from the cylindrical surface of the tube. As the frost develops in time and becomes increasingly more dendritic, the location where the boundary layer transitions to turbulent flow gradually begins to shift toward the front of the coil and more of the evaporator experiences a turbulent flow regime.

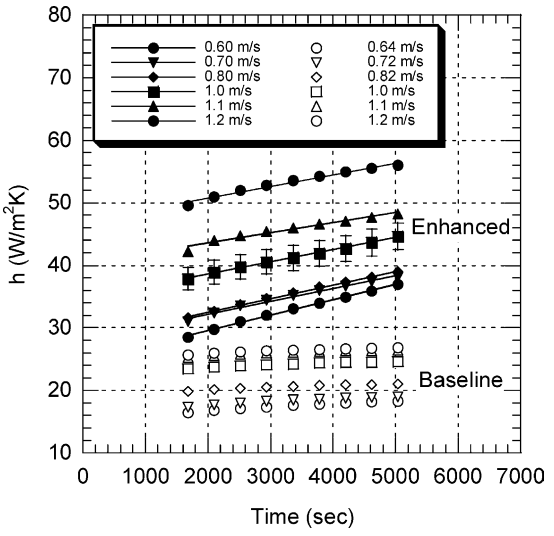

Fig. 9. The heat transfer coefficient is plotted as a function of face velocity and time for frost conditions.

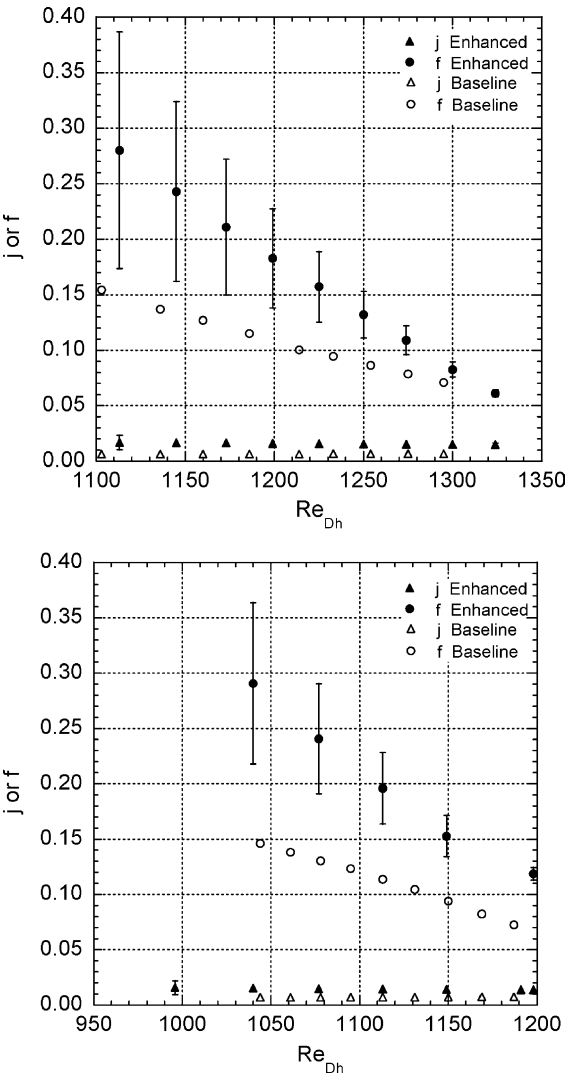

Fig. 10. The j and f factors are both larger for the enhanced geometry under frost conditions.

As this happens, the spatially averaged convective coefficient begins to increase. The second mechanism responsible for this overall increase in the heat transfer coefficient is the narrowing of the air passages due to frost build-up while constant total air mass flow rate is maintained through the coil. The result is an increase in the local air velocity and a reflected increase in the convective coefficient. Third, because the growing frost layer is composed of dendritic spires, the frost may behave as an additional extended surface for heat transfer. In this way, the frost increases the heat transfer surface area of the coil and can produce a small increase in the convective coefficient.

The j factor and friction factor associated with the enhanced geometry under frost conditions are plotted in Fig. 10. First, it should be noted that the j factor associated with the enhanced geometry is everywhere superior to the baseline geometry. Second, it should be noted that the f value for both the enhanced and baseline geometry appears to be approximately the same for small times. Even after 30 min of frost accumulation (which constitutes the first measured f value), the difference between the enhanced and baseline geometry is still relatively small. The friction factor for the enhanced geometry, however, grows at a faster rate than the friction factor for the baseline geometry with the accumulation of frost on the heat exchanger. This difference in the friction factor between the enhanced and baseline geometries is predominantly due to the way the total and minimum free flow areas are calculated. Because the growing frost layer decreases the free flow area of the heat exchanger, the evolving frost thickness plays an important role in determining the airside friction factor. Furthermore, because the frost thickness was found indirectly in these experiments by integrating the frost deposition rate with respect to time to get total mass and then dividing this quantity by the instantaneous frost density found using Hayashi's correlation and the total surface area, there are moderately large uncertainties associated with the friction factor for large times. For this reason, the friction factor data presented in these plots at large times should be used with caution, and the core pressure drop measurements made

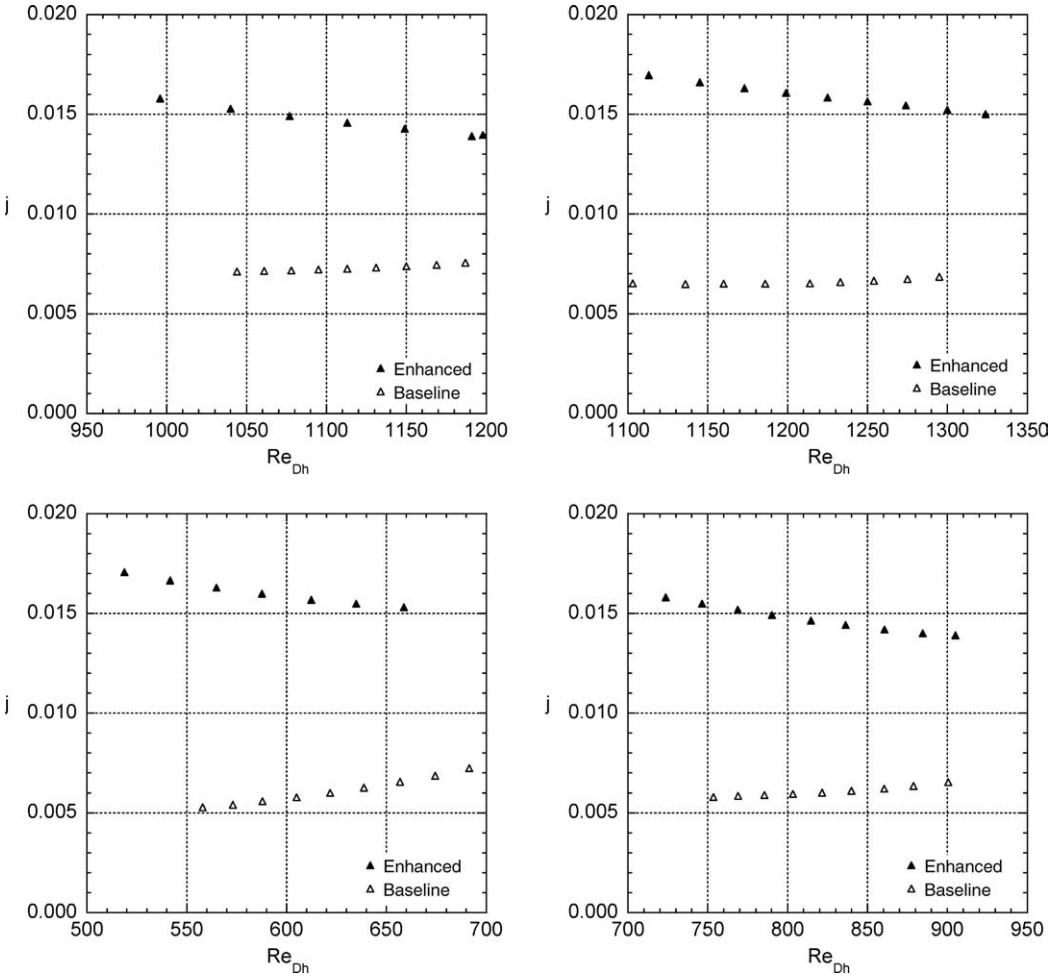

Fig. 11. A closer examination of the j factor shows a large and consistent enhancement over the entire range of Reynolds numbers examined.

under frost conditions (Fig. 7) should be considered as a more accurate assessment of the drag penalty associated with using this VG array under these operating conditions.

In Fig. 11, the *j* factor was examined more closely for Re_{Dh} = 500–1300. Each of these plots constitutes a distinct and unique set of experiments with a different initial face velocity. Therefore, the small differences in the regions of overlap between the plots are attributable to the time-varying history of the frost layer for individual experiments. It is readily apparent, however, that for this range of Reynolds numbers, the *j* factor associated with the enhanced geometry was on average 110–120% larger than the *j* factor for the baseline geometry under equivalent operating conditions. Moreover, there did not appear to be a decrease in the *j* factor difference between the enhanced and baseline cases with decreasing Reynolds numbers. Overall, these results support the convective heat transfer coefficient results presented earlier.

Superimposed on one another in Fig. 12, the baseline data and the enhanced data for the modified volume-goodness factor also exhibited several identifiable trends. First, the thermal hydraulic performance increased with increasing Reynolds number—an observation consistent with expectation. This simple fact confirms that heat transfer is augmented at higher air flow rates. Second, it is important to note that the performance decreased in time as frost accumulated on the evaporator. This degradation is also consistent with what was observed using the London area-goodness factor and emphasizes the frost layer as an additional thermal resistance. Third, the deterioration in thermal performance with time was more pronounced at lower Reynolds numbers. This fact suggests that the properties of the growing frost layer are different at lower Reynolds numbers than at higher Reynolds numbers, which corroborates observation that the frost is more dendritic at lower air flow rates. Dendritic frost, of course, poses a greater conduction resistance than dense frost and might degrade the thermal performance more rapidly, which

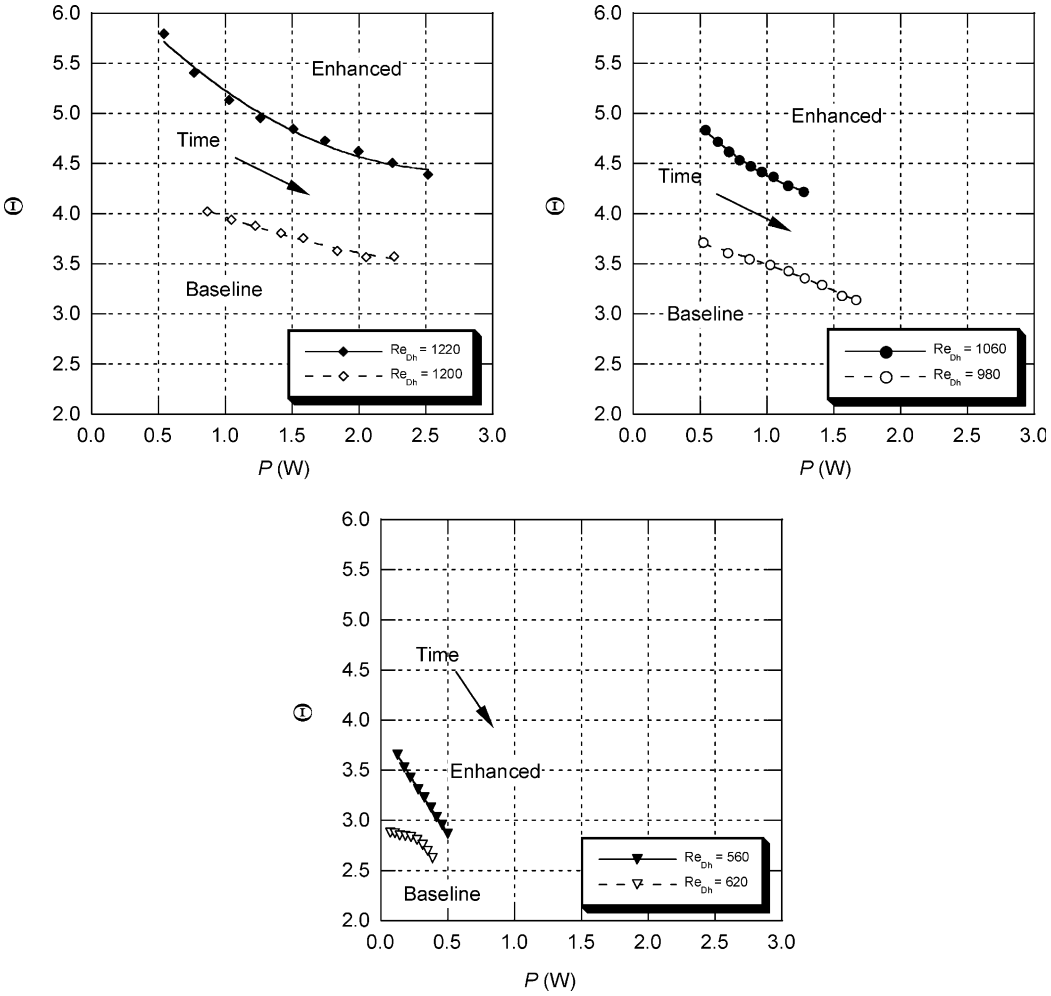

Fig. 12. The modified volume-goodness factor reveals an enhancement of 17–33%.

would explain this trend. It was also readily apparent that using this comparison the VG array was beneficial over the entire range of Reynolds numbers examined. The net enhancement in the volume-goodness factor was 17–33% over the range of face velocities tested. It was also apparent that at low face velocities the magnitude of the difference between the baseline and enhanced data decreases, suggesting no enhancement in the zero-velocity limit. It should be noted that the maximum uncertainty in the modified volume-goodness factor was approximately 2.8%.

The effect of vortex generation on frost properties was also qualitatively examined. As shown in Fig. 13, the average density of the frost layer accumulating on the enhanced evaporator was approximately 30–50 kg m^{-3} greater than the average density on the baseline evaporator. This phenomenon, already observed in channel flow by Storey and Jacobi [6], is probably due to the flow behavior in the downwash region behind the delta wing where the vortex suppresses the axial growth of frost spires and promotes dendritic branching. Because the frost is denser on the enhanced evaporator, the conduction resistance through the frost layer is reduced. This observation was also reflected in the numerically calculated frost thicknesses. The numerically integrated frost thickness on the baseline evaporator was on average 0.4–0.8 mm thicker than the frost layer on the enhanced evaporator. Unlike the instantaneous frost density found using Hayashi's correlation for the purpose of determining the frost thickness, this average frost density was found by dividing the total mass of accumulated frost on the heat exchanger by the surface area and frost thickness. By defining the average frost density in this manner, the dependence of the frost density on the frost surface temperature was reduced. It should be noted that changes in frost density and thermal conductivity might affect defrosting time; however, because no defrost experiments were conducted, we cannot quantify this potential impact. It is relevant to observe that for equal masses of frost on the heat transfer surfaces, it can be expected that defrosting times will be smaller for a more dense frost layer, which will have a higher thermal conductivity than frost in the baseline case.

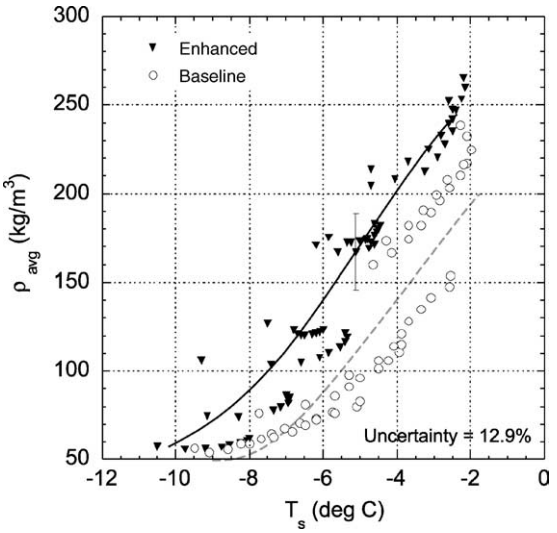

Fig. 13. The average frost density was calculated using measured frost mass deposition data.

5. Conclusions

Predicting the effect that frost has on heat exchanger performance is a difficult and complicated task because of the frost layer sensitivity to substrate wettability, temperature, relative humidity, flow conditions, and growth history. In this study, a full-scale heat exchanger was studied before and after the addition of several delta-wing vortex generators. The specimen heat exchanger was a brazed fin-and-tube evaporator with a fin spacing of 8.5 mm and is currently in production (in an unbrazed version) for use in domestic refrigeration. The examined vortex generator array was a 4-row, staggered configuration where the delta wings were attached in an alternating single row, double row arrangement at a core depth interval of 50.8 mm. For Reynolds numbers between 500 and 1300, which corresponds to face velocities between 0.52 and 1.2 m s^{-1}, the air-side thermal resistance was shown to decrease by 35–42% with the addition of the delta wings, while the convection heat transfer coefficient increased by 60–93%. Typical values for the heat transfer coefficient for the enhanced case were 33–53 W m^{-2} K^{-1}, and typical values for the baseline case were 18–26 W m^{-2} K^{-1}. A modified volume-goodness factor was also calculated and suggested that the delta-wing-enhanced heat exchanger was superior to the baseline heat exchanger over the entire range of Reynolds numbers tested. An average frost density was calculated from mass deposition rate data and revealed that the frost densities were larger for the enhanced case than for the baseline case, suggesting that vortex-induced flow suppresses dendritic frost growth. This conclusion is further supported by the frost thickness data and is an important finding because it suggests that frost grown under enhanced conditions may possess a higher thermal conductivity and therefore may pose a smaller conduction resistance. Based on these results, vortex generation appears to be a viable technique for heat transfer augmentation in these systems. Vortex generation exhibits reasonable tolerance to frost, incurs only a small penalty in pressure drop, and significantly reduces the air-side thermal resistance.

References

[1] M. Fiebig, Vortices, generators, and heat transfer, Trans Inst Chem Eng 76 (A) (1998) 108–123.

[2] K.M. Kwak, K. Torii, K. Nishino, Heat transfer and flow characteristics of fin-tube bundles with and without winglet-type vortex generators, Exp Fluids 33 (2002) 696–702.
[3] C.M.B. Russell, T.V. Jones, G.H. Lee, Heat transfer enhancement using vortex generators, Proceedings of the seventh international heat transfer conference, Munchen, Germany, vol. 3 1982, p. 283–88.
[4] A.I. ElSherbini, A.M. Jacobi, The thermal–hydraulic impact of delta-wing vortex generators on the performance of a plain-fin-and-tube heat exchanger, Int J HVAC R Res 8 (4) (2002) 357–370.
[5] M.C. Gentry, A.M. Jacobi, Heat transfer enhancement by delta-wing vortex generators on a flat plate: vortex interactions with the boundary layer, Exp Therm Fluid Sci 14 (1997) 231–242.
[6] B.D. Storey, A.M. Jacobi, The effect of streamwise vortices on the frost growth rate in developing laminar channel flows, Int J Heat Mass Transfer 42 (1999) 3787–3802.
[7] R. Östin, S. Andersson, Frost growth parameters in a forced air stream, Int J Heat Mass Transfer 34 (5) (1991) 1009–1017.
[8] J.E. White, C.J. Cremers, Prediction of growth parameters of frost deposits in forced convection, J Heat Transfer 103 (1981) 3–6.
[9] R.W. Rite, R.R. Crawford, A parametric study of the factors governing the rate of frost accumulation on domestic refrigerator-freezer finned-tube evaporator coils, ASHRAE Trans 97 (2) (1991) 438–445.
[10] R.W. Rite, R.R. Crawford, The effect of frost accumulation on the performance of domestic refrigerator-freezer finned-tube evaporator coils, ASHRAE Trans 97 (2) (1991) 428–437.
[11] C. Cheng, Y. Cheng, Predictions of frost growth on a cold plate in atmospheric air, Int Commun Heat Mass Transfer 28 (7) (2001) 953–962.
[12] Y. Hayashi, A. Auki, S. Adachi, K. Hori, Study of frost properties correlating with frost formation types, J Heat Transfer 99 (1977) 239–245.
[13] R. Le Gall, J.M. Grillot, Modeling of frost growth and densification, Int J Heat Mass Transfer 40 (13) (1997) 3177–3187.
[14] P.J. Mago, S.A. Sherif, Modeling the cooling process path of a dehumidifying coil under frosting conditions, J Heat Transfer 124 (2002) 1182–1190.
[15] K. Ogawa, N. Tanaka, M. Takeshita, Performance improvement of plate fin-and-tube heat exchangers under frosting conditions, ASHRAE Trans 99 (1) (1993) 762–771.
[16] H.W. Schneider, Equation of the growth rate of frost forming on cooled surfaces, Int J Heat Mass Transfer 21 (1978) 1019–1024.
[17] Y.X. Tao, R.W. Besant, K.S. Rezkallah, A mathematical model for predicting the densification and growth of frost on a flat plate, Int J Heat Mass Transfer 36 (2) (1993) 353–363.
[18] H. Inaba, S. Imai, Study on sublimation phenomenon of horizontal frost layer exposed to forced convection air flow and radiant heat, J Heat Transfer 118 (1996) 694–701.
[19] M.A. Davis, A.M. Jacobi, P.S. Hrnjak, Evaporator calorimeter: the study of overall heat transfer performance. Air Conditioning and Refrigeration Center, ACRC Report TR-107, University of Illinois, Urbana; 1996.
[20] R.K. Shah, A.C. Mueller, Heat exchangers in: W.M. Rohsenow, J.P. Hartnett, E.N. Gani'c (Eds.), Handbook of heat transfer applications, McGraw-Hill, New York, 1985.
[21] K.S. Lee, W.S. Kim, T.H. Lee, A one-dimensional model for frost formation on a cold flat surface, Int J Heat Mass Transfer 40 (18) (1997) 4359–4365.